NANO LETTERS

pubs.acs.org/NanoLett Letter

Ferroelectric Enhanced Performance of a GeSn/Ge Dual-Nanowire Photodetector

Yuekun Yang, Xudong Wang, Chen Wang, Yuxin Song, Miao Zhang, Zhongying Xue, Shumin Wang, Zhongyunshen Zhu, Guanyu Liu, Panlin Li, Linxi Dong, Yongfeng Mei, Paul K. Chu, Weida Hu, Jianlu Wang,* and Zengfeng Di*

Cite This: *Nano Lett.* 2020, 20, 3872−3879 Read Online

ACCESS | Metrics & More | Article Recommendations | Supporting Information

ABSTRACT: GeSn offers a reduced bandgap than Ge and has been utilized in Si-based infrared photodetectors with an extended cutoff wavelength. However, the traditional GeSn/Ge heterostructure usually consists of defects like misfit dislocations due to the lattice mismatch issue. The defects with the large feature size of a photodetector fabricated on bulk GeSn/Ge heterostructures induce a considerable dark current. Here, we demonstrate a flexible GeSn/Ge dual-nanowire (NW) structure, in which the strain relaxation is achieved by the elastic deformation without introducing defects, and the feature dimension is naturally at the nanoscale. A photodetector with a low dark current can be built on a GeSn/Ge dual-NW, which exhibits an extended detection wavelength beyond 2 μm and enhanced responsivity compared to the Ge NW. Moreover, the dark current can be further suppressed by the depletion effect from the ferroelectric polymer side gate. Our work suggests the flexible GeSn/Ge dual-NW may open an avenue for Si-compatible optoelectronic circuits operating in the short-wavelength infrared range.

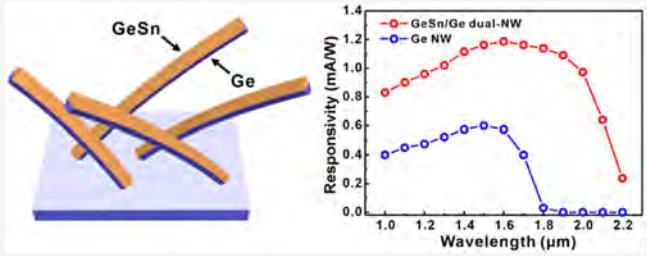

KEYWORDS: *Nanowire, Germanium−tin, Photodetector, Side-gated, Ferroelectrical polymer, Molecular beam epitaxy (MBE)*

Quasi-one-dimensional (1D) semiconducting nanowires (NWs) have been recognized as potential building blocks for optoelectronic devices[1], such as solar cells,[2,3] light-emitting diodes,[4,5] nanolasers,[6,7] and photodetectors[8−11] due to their high surface to volume ratio (S/V). In particular, NW photodetectors operating in the short-wavelength infrared (SWIR) range beyond 2 μm[12] have attracted tremendous interest since SWIR is efficient for data communication, thermal imaging, and molecular vibrations characterization for spectroscopy or biomedical applications.[13−15] Traditional SWIR photodetector technologies are mainly based on HgCdTe, InSb, InGaAs, and other compound semiconductor materials. Due to either the poisonous property or the limited detection wavelength of these compound semiconductor materials (as displayed in Table S1), their application in SWIR technologies[16−18] is still limited. In addition, these compound semiconductor materials are incompatible with the mainstream Si-based complementary metal oxide semiconductor (CMOS) process, which hinders the future development of high-density SWIR photodetectors from integrating with the Si platform.

Ge, as a CMOS compatible group IV semiconductor material, has been considered as a good candidate for a Si-based SWIR detector. However, the light absorption capability of Ge is low due to the indirect bandgap nature, and the cutoff detection wavelength is limited to 1.8 μm due to its bandgap of 0.66 eV.[19−21] By alloying Ge with Sn, the indirect (L) and direct (Γ) valleys in the conduction band of Ge will be lower, and thus, a narrower bandgap can be achieved.[22,23] Therefore, compared to a Ge-based photodetector,[19−21] GeSn has the potential to be utilized as photodetectors with extended detection wavelength, even for mid-infrared ranges.[24−26] Strain-free GeSn alloy displays a direct bandgap nature when Sn concentration is above ∼9%.[27,28] Owing to the reduced bandgap compared to Ge,[29,30] GeSn QWs on Ge buffer have been utilized to build photodetectors with an extended detection wavelength as reported previously.[31−33] However, due to the large lattice mismatch between GeSn and Ge, the compressive strain is always introduced in the GeSn epilayer, and defects like misfit dislocations are easily generated to partially relax the consequent compressive strain,[34−36] which contributes to the dark current of the photodetector built on GeSn QWs. In addition, limited to the resolution of the conventional photolithography process, the feature size of the

Received: March 9, 2020
Revised: April 9, 2020
Published: April 15, 2020

https://dx.doi.org/10.1021/acs.nanolett.0c01039
Nano Lett. 2020, 20, 3872−3879

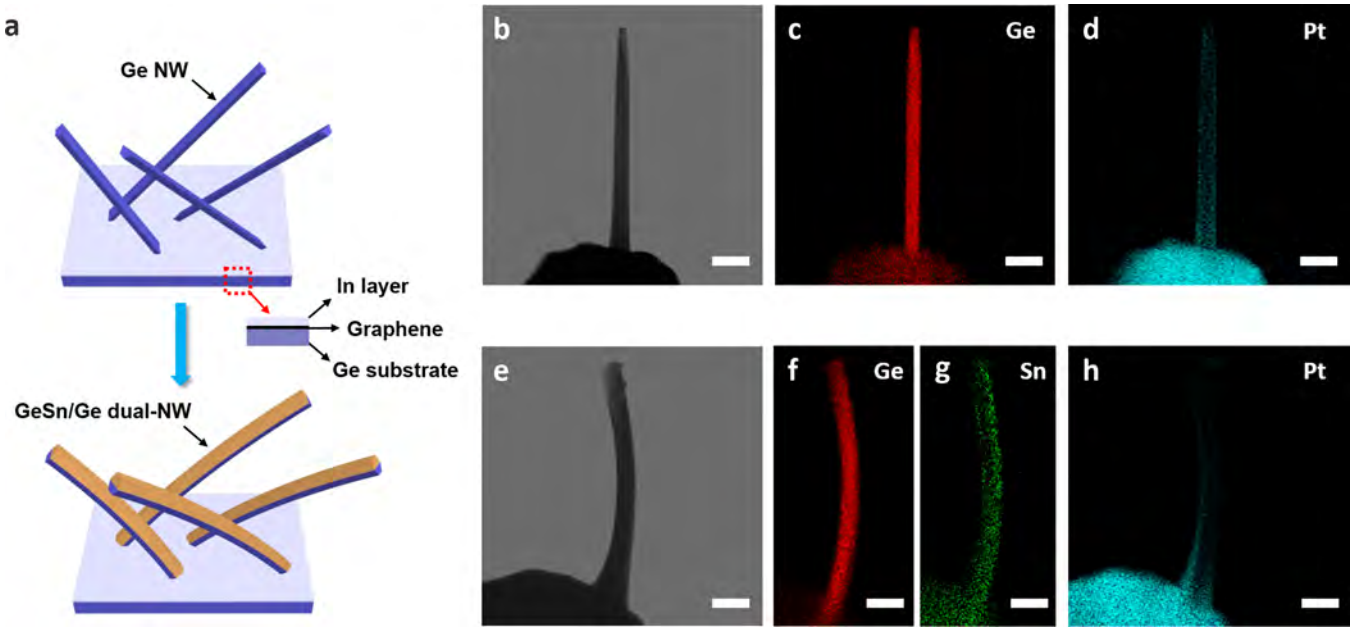

Figure 1. Growth and characterization of the GeSn/Ge dual-nanowires (NWs). (a) The schematic of the GeSn/Ge dual-NWs synthesis process. Inset: Indium layer on graphene acts as a catalyst for Ge NW growth. (b) TEM image of a single Ge NW. The corresponding energy-dispersive X-ray spectroscopy (EDX) mappings of Ge and Pt are shown in panels c and d, respectively. Nonuniform distribution of Pt originates from the TEM sampling process. (e) TEM image of a GeSn/Ge dual-NW. The corresponding EDX mappings of Ge, Sn, and Pt are shown in panels f, g, and h, respectively. Scale bar, 1 μm in b–h.

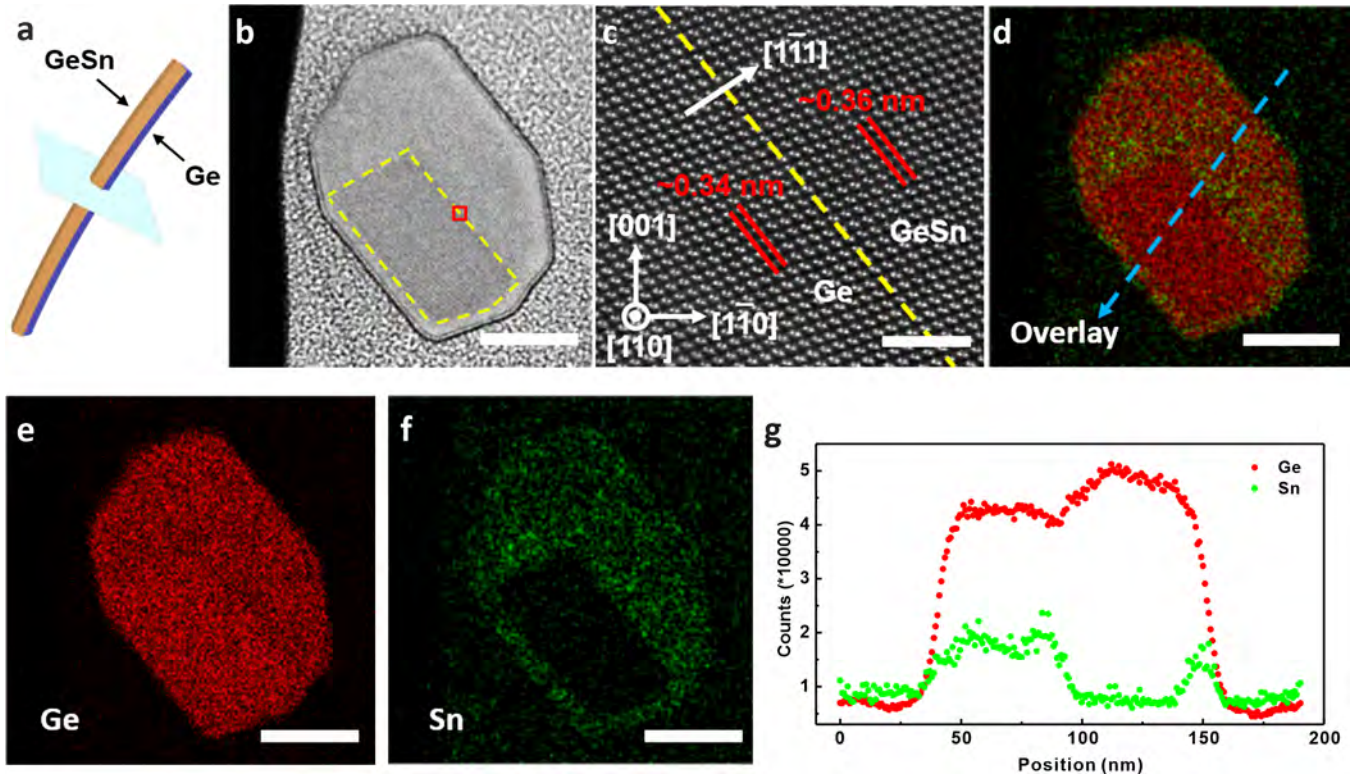

Figure 2. Cross-sectional TEM and EDX compositional mapping of single GeSn/Ge dual-NW. (a) Schematic of a GeSn/Ge dual-NW (The blue plane represents the cross section of the NW). (b) Cross-sectional TEM image of the single GeSn/Ge dual-NW. The yellow dashed rectangle shows the Ge core, and the outer region is the GeSn overlayer. The corresponding EDX mappings of Ge and Sn are shown in panels e and f, respectively. (c) High-resolution TEM image of the red rectangle region shown in panel b. The white arrow indicates the growth direction of GeSn. (d) An overlay EDX mapping of panels e and f. (g) EDX linescan of the blue dashed line in panel d. Scale bar, 50 nm in panels b, d, e, and f, 2 nm in panel c.

GeSn QW photodetector device is relatively large, which induces considerable dark current as well.[31,33] Compared to the photodetector device based on the bulk QW structure, the dimension of the NW counterpart always has a low defect

https://dx.doi.org/10.1021/acs.nanolett.0c01039
Nano Lett. 2020, 20, 3872–3879

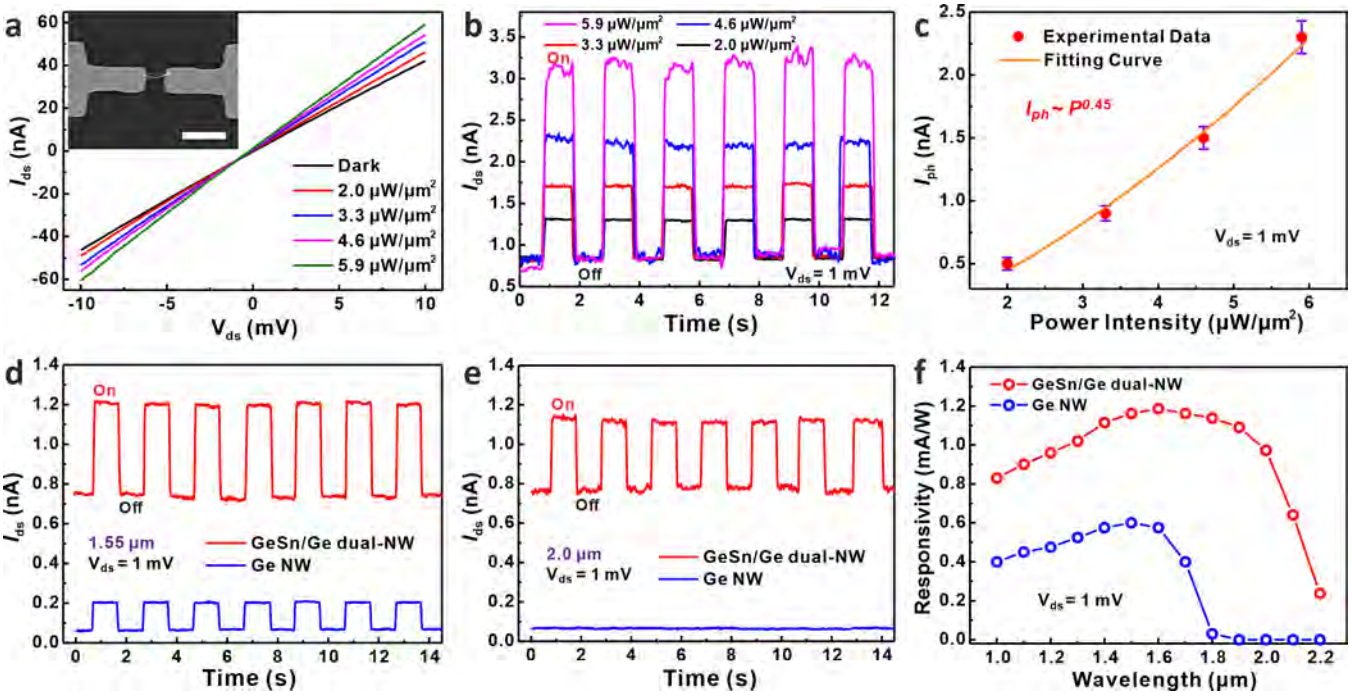

Figure 3. Photoresponse characteristics of the GeSn/Ge dual-NW photodetector. (a) $I_{ds}-V_{ds}$ characteristics of the GeSn/Ge dual-NW device in the dark and under different light intensities (2 μm). Inset: SEM image of the GeSn/Ge dual-NW device with a channel length of 5 μm. (b) Photocurrent response of the device under 2 μm laser light illumination with different intensities at V_{ds} = 1 mV. The light is switched on/off at an interval of 2 s. (c) Dependence of the photocurrent on different light intensities. Error bars represent standard deviations. (d, e) Photoresponse behaviors obtained under 1.55 μm, 2.0 μW/μm^2 laser and 2.0 μm, 2.0 μW/μm^2 laser at V_{ds} = 1 mV, respectively. (f) Spectral responsivities of GeSn/Ge dual-NW and Ge NW photodetector devices under illumination wavelengths from 1.0 to 2.2 μm with a light intensity of 2.0 μW/μm^2 at V_{ds} = 1 mV. Scale bar, 10 μm in panel a.

density and is naturally at the nanoscale, which yields the ultralow dark current, as compared in Table S1. Since the dark current is the main origin of noise and may limit the ability for weak light signal detection, new architecture needs to be integrated with the GeSn system to extend the photodetecting capability to the infrared range with the considerably low dark current.

In this work, we propose and experimentally demonstrate a new flexible dual-NW structure consisting of a GeSn layer with Sn content ~10% heteroepitaxially grown on the sidewall of a Ge NW by molecular beam epitaxy (MBE). Compared to the GeSn/Ge bulk QWs, owing to the flexibility of GeSn/Ge dual-NW, the lattice mismatch induced compressive strain in GeSn can be fully relaxed by the elastic deformation without forming dislocations and defects. Photodetectors based on GeSn/Ge dual-NW are found to exhibit an extended detection range beyond 2 μm and enhanced responsivity compared with the Ge NW counterpart due to the reduced direct bandgap of GeSn.[22,23] Furthermore, due to the nanoscale dimension of the NW structure, the dark current (I_{dc}) of the GeSn/Ge dual-NW photodetector can be reduced, which can be further suppressed by the incorporation of the ferroelectric polymer as a side gate.

The GeSn/Ge dual-NWs were synthesized through a two-step process by MBE as shown in Figure 1a. In the first step, Ge NWs were synthesized on a graphene substrate using the In layer as a catalyst at 570 °C. In the second step, a GeSn overlayer was deposited on the sidewall of the Ge NW at 210 °C, thus forming a dual-layer GeSn/Ge heterostructure NW. The low growth temperature (210 °C) during the second step allows a relatively high growth rate for GeSn, which enables the incorporation of more Sn atoms into Ge lattice without Sn segregation and precipitation due to the low equilibrium solubility of Sn in Ge.[37] In addition, the catalysis capability of In on Ge NW growth was minimized during the second step due to the low temperature, and thus, the GeSn/Ge dual-NW grew thicker rather than longer during the GeSn deposition process (for more details about dual-NW growth, see Supporting Information). Transmission electron microscopy (TEM) images of the Ge NW and GeSn/Ge dual-NW are shown in Figure 1b,e, respectively, together with the corresponding energy-dispersive X-ray spectroscopy (EDX) mapping in Figure 1c,d,f–h. As shown in Figure 1b, the Ge NW is rather straight, suggesting no strain is residual in the Ge NW. In contrast, the GeSn/Ge dual-NW is self-bent, indicating that the compressive strain in GeSn originating from the lattice mismatch between Ge and GeSn is fully relaxed during the formation of the bent GeSn/Ge dual-NW. For the conventional epitaxy of GeSn film on a Ge substrate, the compressive strain in the GeSn layer can only be partially released by forming dislocations at the GeSn/Ge interface, which may increase the dark current and form nonradiative recombination centers. In our study, the GeSn epilayer is deposited on the initial Ge NW with excellent flexibility. Due to the relatively larger lattice constant of GeSn compared to Ge, the GeSn epilayer tends to be compliant to the lattice structure of the Ge core nanowire, which leads to the bending of the GeSn/Ge dual-nanowire as observed. The elastic deformation by the natural bending process enables the strain relaxation process during the growth of the GeSn epilayer on the Ge core NW, which results in the strain-relaxed GeSn/Ge dual-NW.[38]

https://dx.doi.org/10.1021/acs.nanolett.0c01039
Nano Lett. 2020, 20, 3872−3879

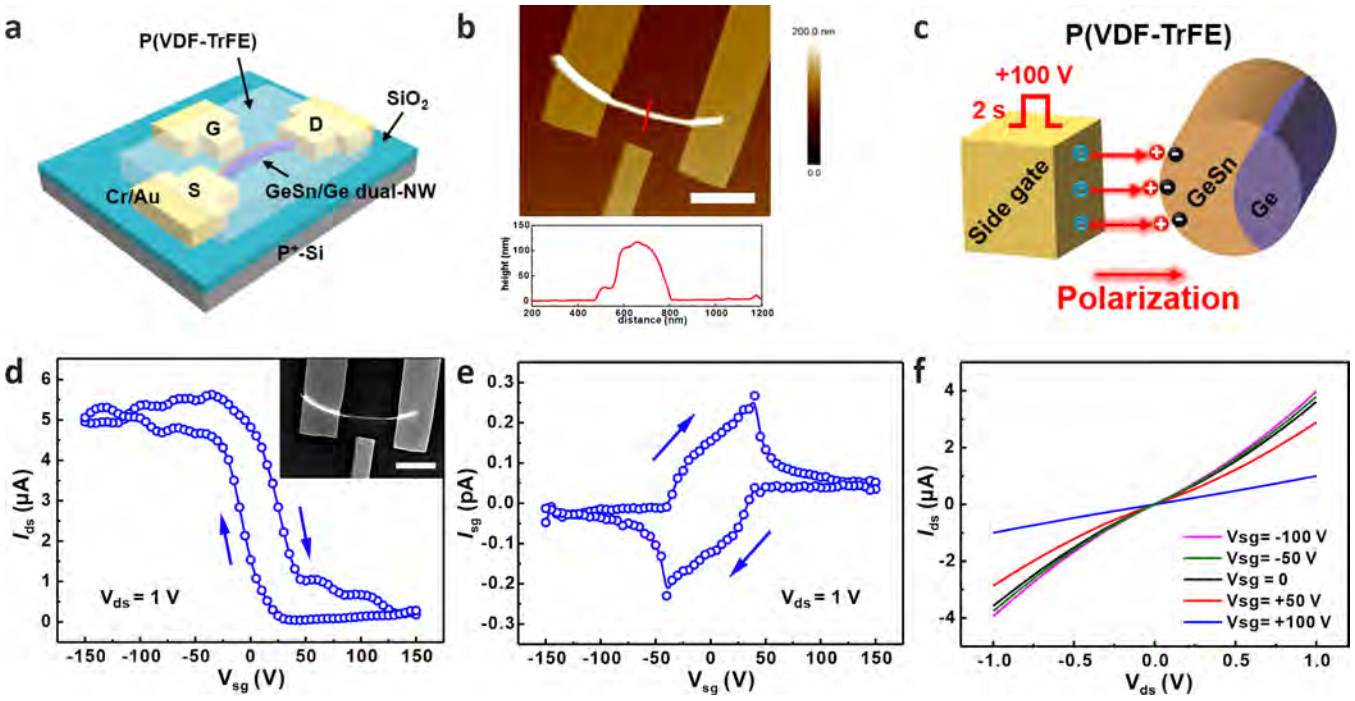

Figure 4. Schematic illustration and electrical properties of a ferroelectric polymer side-gated GeSn/Ge dual-NW device. (a) Three-dimensional schematic view of a ferroelectric polymer side-gated GeSn/Ge dual-NW device. (b) AFM image of the GeSn/Ge dual-NW device. (c) Schematic diagram of the ferroelectric polymer side-gated GeSn/Ge dual-NW device operating in a positive polarization state (depleted state). (d, e) The transfer curves of the GeSn/Ge dual-NW device with the ferroelectric polymer side gate at V_{ds} = 1 V. (Inset in panel d) SEM image of the GeSn/Ge dual-NW device with the side gate. (f) The $I_{ds} - V_{ds}$ characteristics of the ferroelectric polymer side-gated GeSn/Ge dual-NW device at various side gate voltages. Scale bar, 2 μm in panels b and d.

The Sn composition and distribution in the GeSn/Ge dual-NW are studied via cross-sectional EDX mapping in scanning transmission electron microscopy (STEM), as shown in Figure 2. Figure 2a depicts the schematic diagram of the cross section of the GeSn/Ge dual-NW. Figure 2b shows a cross-sectional TEM image of the GeSn/Ge dual-NW presented in Figure 1e, and Figure 2d,e,f corresponds to overlay, Ge, and Sn EDX mapping images, respectively. The yellow dashed rectangle in Figure 2b denotes the contour of the Ge NW core of the GeSn/Ge dual-NW. A uniform Sn distribution is observed in the GeSn region as shown in Figure 2f, indicating that there is no Sn segregation and precipitation in the GeSn alloy. Figure 2g is an EDX linescan along the blue dashed line in Figure 2d. The Sn concentration in GeSn alloy, which is estimated to be ~10% according to the EDX data (see Figure S2), is above the indirect-to-direct bandgap transition threshold at 9%.[27,28] The Sn concentration of the strain-free GeSn/Ge dual-NW is further verified by a 6 cm^{-1} red shift of the Ge−Ge LO mode[39,40] deduced from the comparison of Raman spectroscopy between the Ge NW and the GeSn/Ge dual-NW (see Figure S3). The crystalline structure of the GeSn/Ge dual-NW is revealed by the aberration-corrected high-resolution TEM, as presented in Figure 2c. No defects, such as mismatch dislocations, are observed near the interface between the Ge NW core and the GeSn overlayer. Both Ge and GeSn regions show a single face-centered diamond-cubic lattice structure with high crystalline quality. The white arrow in Figure 2c shows the [1−11] growth direction of the GeSn NW overlayer on top of the Ge NW core. Besides, the interplanar spacing of the GeSn NW overlayer is about 0.36 nm, which is slightly larger than that of the Ge NW (0.34 nm).

The photoresponse characteristics of a single GeSn/Ge dual-NW photodetector are examined under laser excitation with a wavelength of 1.55 and 2.0 μm at an ambient temperature. Figure 3a shows the typical output characteristics of the GeSn/Ge dual-NW photodetector without additional gate voltage. Under the identical positive source−drain voltage (V_{ds}), the light current (I_{lc}) under the illumination of a laser with a 2.0 μm wavelength increases with the increment of light intensity. Figure 3b displays the dynamic photoresponse behaviors of the photodetector under the laser with different incident powers at V_{ds} = 1 mV. The laser with a 2.0 μm wavelength is periodically switched on and off at an interval of 2 s. The GeSn/Ge dual-NW photodetector can respond to the laser pulse very well and exhibits perfect stability and reliability. In addition, the photocurrent (I_{ph}), which can be defined as the difference between I_{lc} and I_{dc}, under a light intensity of 5.9 $\mu W/\mu m^2$ is approximately 4 times larger than that obtained under the light intensity of 2.0 $\mu W/\mu m^2$. I_{ph} exhibits nonlinear increments as the incident light intensity (P) increases at V_{ds} = 1 mV, which can be fitted by the power law relationship of $I_{ph} = cP^k$, where c = 0.34 and k = 0.45 (Figure 3c), as reported previously.[41] The nonlinear dependence of I_{ph} on the incident optical power density indicates that the complex processes occur in the GeSn/Ge dual-NW photodetector, including electron−hole generation, trapping, and recombination.[41,42] Based on the I_{ph} dependence on light power intensity, the responsivity (R) can be further evaluated as ~1.2 mA/W for the GeSn/Ge dual-NW device. Figure 3d,e displays the performance comparison between the GeSn/Ge dual-NW and the Ge NW device under a laser light of 1.55 and 2.0 μm wavelengths, respectively. Compared with the Ge NW photodetector, the GeSn/Ge dual-NW photodetector has a higher responsivity under 1.55 μm

https://dx.doi.org/10.1021/acs.nanolett.0c01039
Nano Lett. 2020, 20, 3872−3879

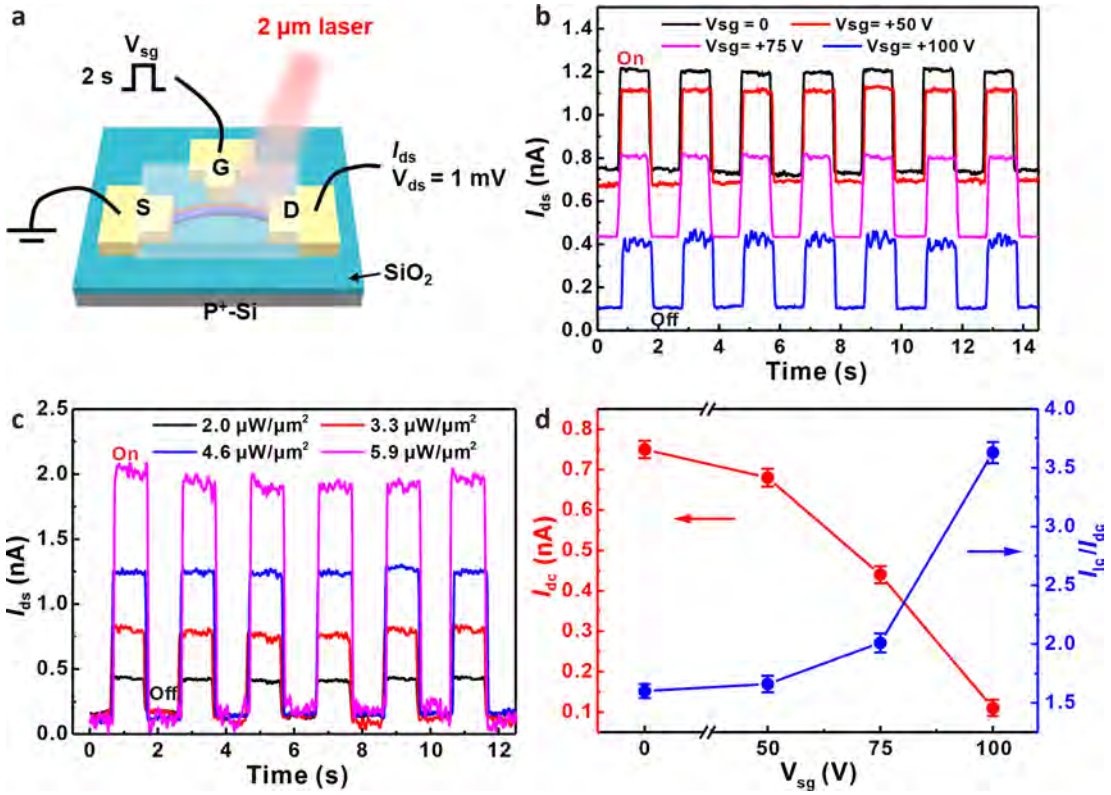

Figure 5. Photoresponse characteristics of a ferroelectric side-gated GeSn/Ge dual-NW photodetector device. (a) Schematic diagram of a ferroelectric side-gated GeSn/Ge dual-NW photodetector device illuminated under the laser. (b) Photocurrent response of the photodetector device under 2.0 μm, 2.0 $\mu W/\mu m^2$ laser with an interval of 2 s after different positive side gate polarizations at V_{ds} = 1 mV. (c) Photocurrent response of the +100 V side-gated photodetector device under laser illumination (2.0 μm) with different intensities at V_{ds} = 1 mV. The laser is switched on/off at an interval of 2 s. (d) Dependences of I_{dc} and the I_{lc}/I_{dc} (on/off) ratio on the side gate voltage under 2.0 μm, 2.0 $\mu W/\mu m^2$ laser illumination. Error bars represent standard deviations.

illumination, which is believed to be due to the direct bandgap nature and enhanced light absorption capability of the GeSn NW in the GeSn/Ge dual-NW. In addition, due to the reduced bandgap of GeSn, the detection wavelength can be extended to 2.0 μm for the GeSn/Ge dual-NW photodetector, as shown in Figure 3e. However, no photoresponse is observed in the Ge NW photodetector under the identical 2.0 μm illumination. Figure 3f depicts the spectral response of two detectors under the illumination with the light intensity of 2.0 $\mu W/\mu m^2$ at a bias of 1 mV and the wavelength varying from 1.0 to 2.2 μm. It is found that, for the Ge NW device, the maximum value of responsivity is obtained at ~1.5 μm. The responsivity declines dramatically when the wavelength is longer than 1.5 μm, and it approaches nearly zero for the wavelength beyond 1.8 μm. The cutoff wavelength, i.e., 1.8 μm, is consistent with the bandgap value of pure Ge. On the contrary, the GeSn/Ge dual-NW detector has an appreciable photoresponse even at a wavelength of 2.2 μm. The extended photoresponse wavelength can be attributed to the reduced bandgap of GeSn in the GeSn/Ge dual-NW compared to Ge NW. It is worth noticing that the reduced bandgap of GeSn also induces the undesirable increment of dark currents (I_{dc}) in the GeSn/Ge dual-NW under the illumination of a laser with a wavelength of 1.55 or 2.0 μm[43] (Figure 3d,e), which decreases the I_{lc}/I_{dc} ratio (on/off ratio) of the corresponding photodetector, thus degrading the detection performance.

The suppression of the dark current is essential to increase the I_{lc}/I_{dc} ratio, thus improving the detectivity of high-performance photodetection.[41,44] In order to reduce I_{dc} of the GeSn/Ge dual-NW photodetector, poly(vinylidene fluoride-trifluoroethylene) P(VDF-TrFE) is used as the ferroelectric side gate dielectric for GeSn/Ge dual-NW photodetectors (see Supporting Information, Section I, for more details). The schematic diagram and the corresponding atomic force microscopy (AFM) image of ferroelectric side-gated GeSn/Ge dual-NW photodetector are depicted in Figure 4a and b, respectively. The inset of Figure 4d shows the corresponding SEM image of the photodetector device. As the positive bias is applied on the side gate electrode, the polarization of the ferroelectric film will be aligned to the NW under the positive electrostatic field gradient, as schematically drawn in Figure 4c. The $I_{ds} - V_{sg}$ and $I_{sg} - V_{sg}$ transfer characteristics of the GeSn/Ge dual-NW device are shown in Figure 4d,e, respectively. Both curves clearly demonstrate the ferroelectric hysteresis nature of the P(VDF-TrFE). The side gate current (I_{sg}) is on the order of pA even when the side gate voltage (V_{sg}) exceeds ±100 V, indicating that the P(VDF-TrFE) is working well without breakdown even at high V_{sg}. For the positive polarization state, the source−drain current (I_{ds}) decreases as the positive bias applied on the side gate electrode increases, as shown in Figure 4f. As +100 V is applied on the side gate, I_{ds} at V_{ds} = 1 V is shrunk to ~15% of that obtained from the GeSn/Ge dual-NW photodetector with V_{sg} = 0 V. It indicates that, after applying a positive side gate voltage, the electrostatic field derived from the remnant polarization of P(VDF-TrFE) results in depletion of the holes (majority carriers) of the p-type GeSn/Ge dual-NW. However, when the ferroelectric dielectric changes into the negative polarization state, I_{ds} will barely

https://dx.doi.org/10.1021/acs.nanolett.0c01039
Nano Lett. 2020, 20, 3872−3879

respond to the variation of the negative bias applied on the side gate electrode, indicating that the negative polarization state corresponds to the depletion of the electrons (minority carriers) in the GeSn/Ge dual-NW.[45] Therefore, it implies that the positive bias applied to the ferroelectric polymer side gate can be further utilized to reduce the dark current (I_{dc}) of the GeSn/Ge dual-NW detector.

To validate the effect of the ferroelectric polymer side gate on the reduction of I_{dc}, photoresponse behaviors of the GeSn/Ge dual-NW photodetector are investigated under the positive polarization in detail, as displayed in Figure 5a. Photocurrent response behaviors under a 2.0 $\mu W/\mu m^2$ chopped laser with a wavelength of 2.0 μm before and after different positive side gate polarizations are displayed in Figure 5b. It is obvious that I_{dc} decreases significantly with the gradual increment of the side gate pulse voltage. As +100 V bias with the pulse of 2 s is applied on the side gate, the I_{dc} of the GeSn/Ge dual-NW photodetector is reduced to ~0.1 nA (comparable to NW photodetectors based on other semiconductor materials as displayed in Table S1), which is reduced 85% compared to the value obtained at V_{sg} = 0 V and even lower than that of the Ge NW device obtained under the illumination of a 1.55 μm laser with the same measurement condition (Figure 3b). Figure 5c presents the photoresponse of the GeSn/Ge dual-NW detector with +100 V side gate polarization toward chopped laser illumination (2 μm) of different light intensities. It is found that, different from I_{lc}, I_{dc} is not sensitive to the intensity of excitation laser and always suppressed regardless of the laser intensity. Even the laser intensity increases to 5.9 $\mu W/\mu m^2$; the value of I_{dc} is still as low as 0.1 nA. To further investigate the ferroelectric polymer side gate effect, the dependences of I_{dc} and the I_{lc}/I_{dc} ratio (on/off ratio) on the side gate voltage are statistically presented in Figure 5d. It is observed that I_{dc} of the GeSn/Ge dual-NW photodetector can be manipulated by the bias at the ferroelectric polymer side gate, and the appreciably low I_{dc} can be obtained at a high side gate voltage. Furthermore, the I_{lc}/I_{dc} ratio of the GeSn/Ge dual-NW photodetector can also be improved significantly by the increment of side gate voltage. Therefore, with the integration of the ferroelectric polymer side gate and GeSn/Ge dual-NW, the photodetector with the extended detection range and the improved detectivity can be obtained.

In summary, we demonstrate a high-performance photodetector based on the GeSn/Ge dual-NW that possesses an extended detection wavelength up to 2.2 μm compared with the Ge NW counterpart. Furthermore, assisted by the ferroelectric polymer side gate, the undesirable dark current of the GeSn/Ge dual-NW photodetector can be effectively suppressed by 85%; therefore, its detectivity can be considerably enhanced correspondingly. Our strategy relying on the conjunction of the ferroelectric polymer side gate and GeSn/Ge dual-NW may open a new avenue to explore photodetection application based on group IV semiconductor materials.

METHODS

Nanowire Synthesis and Characterization. The GeSn/Ge dual-NWs were synthesized using the DCA P450 MBE system via a two-step process. First, the graphene-coated Ge substrate was smeared with a thick In layer and heated by a hot plate (200 °C) for 2 min prior to the transfer into the MBE growth chamber. Then, the first step for Ge NW growth started with the Ge flow flux of 0.012 nm/s at 570 °C and continued for 150 min. After the growth of the Ge NW, the second step for the GeSn overlayer growth subsequently started at 210 °C with Ge flux of 0.1 nm/s and Sn flux of 0.015 nm/s and continued for 850 s to form the GeSn/Ge dual-NW with a diameter of ~150−200 nm and a length of 8−10 μm. The morphologies of GeSn/Ge dual-NWs were characterized by SEM (HITACHI-S4700) and AFM (Bruker, Multimode 8). The Sn concentration in the GeSn/Ge dual-NW was estimated by Raman spectroscopy (HORIBA Jobin Yvon HR800) using an Ar^+ laser with a wavelength of 514 nm and STEM together with EDX mapping (aberration-corrected JEM-ARM300F system) with an accelerating voltage of 300 kV.

Device Fabrication and Measurement. The GeSn/Ge dual-NWs were mechanically transferred to the SiO_2/Si substrate (300 nm SiO_2). Then, the substrate was spin-coated with methyl methacrylate (MMA) and poly(methyl methacrylate) (PMMA), and electron-beam lithography (Zeiss Sigma system) was utilized to define the areas for drain, source, and side-gated electrodes. The Cr/Au (5 nm/45 nm) electrodes were deposited via e-beam metal evaporation (Kurt J. Lesker system). Ferroelectric polymer P(VDF-TrFE) (200 nm thick) was deposited on the NW channels by spin-coating. Afterward, the P(VDF-TrFE) layer was annealed at 130 °C for 2 h on a hot plate to improve its crystallinity. The optoelectronic measurements of NW devices were performed in a Lake Shore TTPX probe station connected to a Keithly 4200 semiconductor characterization system at an ambient temperature.

ASSOCIATED CONTENT

Supporting Information

The Supporting Information is available free of charge at https://pubs.acs.org/doi/10.1021/acs.nanolett.0c01039.

Review of photodetector devices built on different materials and structures; nanowire synthesis; experimental procedure; characterization of Ge NW and GeSn/Ge dual-NW; SEM images of various substrates after Ge NW growth; Sn composition in GeSn/Ge dual-NW; surface morphologies and Raman spectra of Ge NW and GeSn/Ge dual-NW (PDF)

AUTHOR INFORMATION

Corresponding Authors

Jianlu Wang − *State Key Laboratory for Infrared Physics, Shanghai Institute of Technical Physics, Chinese Academy of Sciences, Shanghai 200083, China;* orcid.org/0000-0002-5029-8728; Email: jlwang@mail.sitp.ac.cn

Zengfeng Di − *State Key Laboratory of Functional Materials for Informatics, Shanghai Institute of Microsystem and Information Technology, Chinese Academy of Sciences, Shanghai 200050, China;* orcid.org/0000-0002-9357-5107; Email: zfdi@mail.sim.ac.cn

Authors

Yuekun Yang − *State Key Laboratory of Functional Materials for Informatics, Shanghai Institute of Microsystem and Information Technology, Chinese Academy of Sciences, Shanghai 200050, China; Center of Materials Science and Optoelectronics Engineering, University of Chinese Academy of Sciences, Beijing 100049, China*

https://dx.doi.org/10.1021/acs.nanolett.0c01039
Nano Lett. 2020, 20, 3872−3879

Xudong Wang − *State Key Laboratory for Infrared Physics, Shanghai Institute of Technical Physics, Chinese Academy of Sciences, Shanghai 200083, China*
Chen Wang − *State Key Laboratory of Functional Materials for Informatics, Shanghai Institute of Microsystem and Information Technology, Chinese Academy of Sciences, Shanghai 200050, China;* orcid.org/0000-0002-4749-8091
Yuxin Song − *State Key Laboratory of Functional Materials for Informatics, Shanghai Institute of Microsystem and Information Technology, Chinese Academy of Sciences, Shanghai 200050, China*
Miao Zhang − *State Key Laboratory of Functional Materials for Informatics, Shanghai Institute of Microsystem and Information Technology, Chinese Academy of Sciences, Shanghai 200050, China*
Zhongying Xue − *State Key Laboratory of Functional Materials for Informatics, Shanghai Institute of Microsystem and Information Technology, Chinese Academy of Sciences, Shanghai 200050, China*
Shumin Wang − *State Key Laboratory of Functional Materials for Informatics, Shanghai Institute of Microsystem and Information Technology, Chinese Academy of Sciences, Shanghai 200050, China*
Zhongyunshen Zhu − *State Key Laboratory of Functional Materials for Informatics, Shanghai Institute of Microsystem and Information Technology, Chinese Academy of Sciences, Shanghai 200050, China*
Guanyu Liu − *State Key Laboratory of Functional Materials for Informatics, Shanghai Institute of Microsystem and Information Technology, Chinese Academy of Sciences, Shanghai 200050, China*
Panlin Li − *State Key Laboratory of Functional Materials for Informatics, Shanghai Institute of Microsystem and Information Technology, Chinese Academy of Sciences, Shanghai 200050, China*
Linxi Dong − *Key Laboratory of RF Circuits and System of Ministry of Education, College of Electronic and Information, Hangzhou Dianzi University, Hangzhou 310018, China*
Yongfeng Mei − *Department of Materials Science, State Key Laboratory of ASIC and Systems, Fudan University, Shanghai 200433, China;* orcid.org/0000-0002-3314-6108
Paul K. Chu − *Department of Physics, Department of Materials Science & Engineering, and Department of Biomedical Engineering, City University of Hong Kong, Kowloon, Hong Kong, China;* orcid.org/0000-0002-5581-4883
Weida Hu − *State Key Laboratory for Infrared Physics, Shanghai Institute of Technical Physics, Chinese Academy of Sciences, Shanghai 200083, China;* orcid.org/0000-0001-5278-8969

Complete contact information is available at: https://pubs.acs.org/10.1021/acs.nanolett.0c01039

Author Contributions

Y.Y., Y.S., S.W., W.H., J.W., and Z.D. designed the experiments. Y.Y., X.W., and Z.Z performed nanowire growth experiments and characterization. Y.Y., G.L., and X.W. fabricated the device and carried out the measurements. Y.Y., C.W., J.W., and Z.D. cowrote the paper. S.W., P.K.C., W.H., J.W., and Z.D. conceived and supervised the research. All authors discussed the results and revised the manuscript.

Notes

The authors declare no competing financial interest.

■ ACKNOWLEDGMENTS

The authors thank Key Research Project of Frontier Science, Chinese Academy of Sciences (QYZDB-SSW-JSC021), National Science and Technology Major Project (2016ZX02301003), National Natural Science Foundation of China (51925208, 61974157, and 61851401), Strategic Priority Research Program (B) of the Chinese Academy of Sciences (XDB30030000).

■ REFERENCES

(1) Duan, X. F.; Huang, Y.; Cui, Y.; Wang, J. F.; Lieber, C. M. Indium Phosphide Nanowires as Building Blocks for Nanoscale Electronic and Optoelectronic Devices. *Nature* **2001**, *409*, 66−69.
(2) Wallentin, J.; Anttu, N.; Asoli, D.; Huffman, M.; Aberg, I.; Magnusson, M. H.; Siefer, G.; Fuss-Kailuweit, P.; Dimroth, F.; Witzigmann, B.; Xu, H. Q.; Samuelson, L.; Deppert, K.; Borgstrom, M. T. InP Nanowire Array Solar Cells Achieving 13.8% Efficiency by Exceeding the Ray Optics Limit. *Science* **2013**, *339*, 1057−1060.
(3) Li, L.; Lu, H.; Yang, Z.; Tong, L.; Bando, Y.; Golberg, D. Bandgap-Graded CdS_xSe_{1-x} Nanowires for High-Performance Field-Effect Transistors and Solar Cells. *Adv. Mater.* **2013**, *25*, 1109−1113.
(4) Gudiksen, M. S.; Lauhon, L. J.; Wang, J.; Smith, D. C.; Lieber, C. M. Growth of Nanowire Superlattice Structures for Nanoscale Photonics and Electronics. *Nature* **2002**, *415*, 617−620.
(5) Tomioka, K.; Motohisa, J.; Hara, S.; Hiruma, K.; Fukui, T. GaAs/AlGaAs Core Multishell Nanowire-Based Light-Emitting Diodes on Si. *Nano Lett.* **2010**, *10*, 1639−1644.
(6) Duan, X. F.; Huang, Y.; Agarwal, R.; Lieber, C. M. Single-Nanowire Electrically Driven Lasers. *Nature* **2003**, *421*, 241−245.
(7) Saxena, D.; Wang, F.; Gao, Q.; Mokkapati, S.; Tan, H. H.; Jagadish, C. Mode Profiling of Semiconductor Nanowire Lasers. *Nano Lett.* **2015**, *15*, 5342−5348.
(8) Liu, X.; Gu, L.; Zhang, Q.; Wu, J.; Long, Y.; Fan, Z. All-Printable Band-Edge Modulated ZnO Nanowire Photodetectors with Ultra-High Detectivity. *Nat. Commun.* **2014**, *5*, 4007.
(9) Guo, N.; Hu, W.; Liao, L.; Yip, S.; Ho, J. C.; Miao, J.; Zhang, Z.; Zou, J.; Jiang, T.; Wu, S.; Chen, X.; Lu, W. Anomalous and Highly Efficient InAs Nanowire Phototransistors Based on Majority Carrier Transport at Room Temperature. *Adv. Mater.* **2014**, *26*, 8203−8209.
(10) Liu, Z.; Luo, T.; Liang, B.; Chen, G.; Yu, G.; Xie, X.; Chen, D.; Shen, G. High-Detectivity InAs Nanowire Photodetectors with Spectral Response from Ultraviolet to Near-Infrared. *Nano Res.* **2013**, *6*, 775−783.
(11) Peng, K.; Parkinson, P.; Fu, L.; Gao, Q.; Jiang, N.; Guo, Y. N.; Wang, F.; Joyce, H. J.; Boland, J. L.; Tan, H. H.; Jagadish, C.; Johnston, M. B. Single Nanowire Photoconductive Terahertz Detectors. *Nano Lett.* **2015**, *15*, 206−210.
(12) Hansen, M.; Malchow, D. Overview of SWIR Detectors, Cameras, and Applications. *SPIE Defense and Security Symposium*; SPIE, 2008; Vol. *6939*.
(13) Hu, Y. F.; Zhou, J.; Yeh, P. H.; Li, Z.; Wei, T. Y.; Wang, Z. L. Supersensitive, Fast-Response Nanowire Sensors by Using Schottky Contacts. *Adv. Mater.* **2010**, *22*, 3327−3332.
(14) Zou, X.; Wang, J.; Liu, X.; Wang, C.; Jiang, Y.; Wang, Y.; Xiao, X.; Ho, J. C.; Li, J.; Jiang, C.; Fang, Y.; Liu, W.; Liao, L. Rational Design of Sub-Parts per Million Specific Gas Sensors Array Based on Metal Nanoparticles Decorated Nanowire Enhancement-Mode Transistors. *Nano Lett.* **2013**, *13*, 3287−3292.
(15) Sun, J.; Peng, M.; Zhang, Y.; Zhang, L.; Peng, R.; Miao, C.; Liu, D.; Han, M.; Feng, R.; Ma, Y.; Dai, Y.; He, L.; Shan, C.; Pan, A.; Hu, W.; Yang, Z.-x. Ultrahigh Hole Mobility of Sn-Catalyzed GaSb Nanowires for High Speed Infrared Photodetectors. *Nano Lett.* **2019**, *19*, 5920−5929.
(16) Cuesta, S.; Spies, M.; Boureau, V.; Donatini, F.; Hocevar, M.; den Hertog, M. I.; Monroy, E. Effect of Bias on the Response of GaN Axial p−n Junction Single-Nanowire Photodetectors. *Nano Lett.* **2019**, *19*, 5506−5514.

(17) Luo, W.; Weng, Q.; Long, M.; Wang, P.; Gong, F.; Fang, H.; Luo, M.; Wang, W.; Wang, Z.; Zheng, D.; Hu, W.; Chen, X.; Lu, W. Room-Temperature Single-Photon Detector Based on Single Nanowire. *Nano Lett.* **2018**, *18*, 5439−5445.
(18) Zheng, D. S.; Fang, H. H.; Long, M. S.; Wu, F.; Wang, P.; Gong, F.; Wu, X.; Ho, J. C.; Liao, L.; Hu, W. D. High-Performance Near-Infrared Photodetectors Based on P-Type SnX (X = S, Se) Nanowires Grown via Chemical Vapor Deposition. *ACS Nano* **2018**, *12*, 7239−7245.
(19) Otuonye, U.; Kim, H. W.; Lu, W. D. Ge Nanowire Photodetector with High Photoconductive Gain Epitaxially Integrated on Si Substrate. *Appl. Phys. Lett.* **2017**, *110*, 173104.
(20) Lee, H.-S.; Kim, C.-J.; Lee, D.; Lee, R. R.; Kang, K.; Hwang, I.; Jo, M.-H. Large Electroabsorption Susceptibility Mediated by Internal Photoconductive Gain in Ge Nanowires. *Nano Lett.* **2012**, *12*, 5913−5918.
(21) Staudinger, P.; Sistani, M.; Greil, J.; Bertagnolli, E.; Lugstein, A. Ultrascaled Germanium Nanowires for Highly Sensitive Photodetection at the Quantum Ballistic Limit. *Nano Lett.* **2018**, *18*, 5030−5035.
(22) Gupta, S.; Chen, R.; Huang, Y.-C.; Kim, Y.; Sanchez, E.; Harris, J. S.; Saraswat, K. C. Highly Selective Dry Etching of Germanium over Germanium−Tin ($Ge_{1-x}Sn_x$): A Novel Route for $Ge_{1-x}Sn_x$ Nanostructure Fabrication. *Nano Lett.* **2013**, *13*, 3783−3790.
(23) Chen, R.; Gupta, S.; Huang, Y. C.; Huo, Y. J.; Rudy, C. W.; Sanchez, E.; Kim, Y.; Kamins, T. I.; Saraswat, K. C.; Harris, J. S. Demonstration of a Ge/GeSn/Ge Quantum-Well Microdisk Resonator on Silicon: Enabling High-Quality Ge(Sn) Materials for Micro- and Nanophotonics. *Nano Lett.* **2014**, *14*, 37−43.
(24) Meng, A. C.; Fenrich, C. S.; Braun, M. R.; McVittie, J. P.; Marshall, A. F.; Harris, J. S.; McIntyre, P. C. Core-Shell Germanium/Germanium−Tin Nanowires Exhibiting Room-Temperature Direct- and Indirect-Gap Photoluminescence. *Nano Lett.* **2016**, *16*, 7521−7529.
(25) Assali, S.; Dijkstra, A.; Li, A.; Koelling, S.; Verheijen, M. A.; Gagliano, L.; von den Driesch, N.; Buca, D.; Koenraad, P. M.; Haverkort, J. E. M.; Bakkers, E. P. A. M. Growth and Optical Properties of Direct Band Gap $Ge/Ge_{0.87}Sn_{0.13}$ Core/Shell Nanowire Arrays. *Nano Lett.* **2017**, *17*, 1538−1544.
(26) Seifner, M. S.; Dijkstra, A.; Bernardi, J.; Steiger-Thirsfeld, A.; Sistani, M.; Lugstein, A.; Haverkort, J. E. M.; Barth, S. Epitaxial $Ge_{0.81}Sn_{0.19}$ Nanowires for Nanoscale Mid-Infrared Emitters. *ACS Nano* **2019**, *13*, 8047−8054.
(27) Biswas, S.; Doherty, J.; Saladukha, D.; Ramasse, Q.; Majumdar, D.; Upmanyu, M.; Singha, A.; Ochalski, T.; Morris, M. A.; Holmes, J. D. Non-Equilibrium Induction of Tin in Germanium: Towards Direct Bandgap $Ge_{1-x}Sn_x$ Nanowires. *Nat. Commun.* **2016**, *7*, 11405.
(28) Doherty, J.; Biswas, S.; McNulty, D.; Downing, C.; Raha, S.; O'Regan, C.; Singha, A.; O'Dwyer, C.; Holmes, J. D. One-Step Fabrication of GeSn Branched Nanowires. *Chem. Mater.* **2019**, *31*, 4016−4024.
(29) Geiger, R.; Zabel, T.; Sigg, H. Group IV Direct Band Gap Photonics: Methods, Challenges, and Opportunities. *Front. Mater.* **2015**, *2*, 52.
(30) Kasper, E.; Kittler, M.; Oehme, M.; Arguirov, T. Germanium Tin: Silicon Photonics Toward the Mid-Infrared [Invited]. *Photonics Res.* **2013**, *1*, 69−76.
(31) Gassenq, A.; Gencarelli, F.; Van Campenhout, J.; Shimura, Y.; Loo, R.; Narcy, G.; Vincent, B.; Roelkens, G. GeSn/Ge Heterostructure Short-wave Infrared Photodetectors on Silicon. *Opt. Express* **2012**, *20*, 27297−27303.
(32) Tran, H.; Pham, T.; Margetis, J.; Zhou, Y.; Dou, W.; Grant, P. C.; Grant, J. M.; Al-Kabi, S.; Sun, G.; Soref, R. A.; Tolle, J.; Zhang, Y.-H.; Du, W.; Li, B.; Mortazavi, M.; Yu, S.-Q. Si-Based GeSn Photodetectors toward Mid-Infrared Imaging Applications. *ACS Photonics* **2019**, *6*, 2807−2815.
(33) Pham, T.; Du, W.; Tran, H.; Margetis, J.; Tolle, J.; Sun, G.; Soref, R. A.; Naseem, H. A.; Li, B.; Yu, S.-Q. Systematic Study of Si-based GeSn Photodiodes with 2.6 μm Detector Cutoff for Short-wave Infrared Detection. *Opt. Express* **2016**, *24*, 4519−4531.
(34) Senaratne, C. L.; Wallace, P. M.; Gallagher, J. D.; Sims, P. E.; Kouvetakis, J.; Menéndez, J. Direct Gap $Ge_{1-y}Sn_y$ Alloys: Fabrication and Design of Mid-IR Photodiodes. *J. Appl. Phys.* **2016**, *120*, 025701.
(35) Oehme, M.; Buca, D.; Kostecki, K.; Wirths, S.; Holländer, B.; Kasper, E.; Schulze, J. Epitaxial Growth of Highly Compressively Strained GeSn Alloys up to 12.5% Sn. *J. Cryst. Growth* **2013**, *384*, 71−76.
(36) Dong, Y.; Wang, W.; Lee, S. Y.; Lei, D.; Gong, X.; Loke, W. K.; Yoon, S.-F.; Liang, G.; Yeo, Y.-C. Germanium-Tin Multiple Quantum Well on Silicon Avalanche Photodiode for Photodetection at Two Micron Wavelength. *Semicond. Sci. Technol.* **2016**, *31*, 095001.
(37) Sun, Y.-L.; Matsumura, R.; Jevasuwan, W.; Fukata, N. Au−Sn Catalyzed Growth of $Ge_{1-x}Sn_x$ Nanowires: Growth Direction, Crystallinity, and Sn Incorporation. *Nano Lett.* **2019**, *19*, 6270−6277.
(38) Yu, J. L.; Chen, Y. H.; Liu, Y.; Cheng, S. Y. Effects of Strain in Low-Dimensional Semiconductor Structures. *Nanosci. Nanotechnol. Lett.* **2017**, *9*, 1066−1082.
(39) Han, D.; Ye, H.; Song, Y.; Zhu, Z.; Yang, Y.; Yu, Z.; Liu, Y.; Wang, S.; Di, Z. Analysis of Raman Scattering from Inclined GeSn/Ge Dual-Nanowire Heterostructure on Ge(111) Substrate. *Appl. Surf. Sci.* **2019**, *463*, 581−586.
(40) Gassenq, A.; Milord, L.; Aubin, J.; Pauc, N.; Guilloy, K.; Rothman, J.; Rouchon, D.; Chelnokov, A.; Hartmann, J. M.; Reboud, V.; Calvo, V. Raman Spectral Shift versus Strain and Composition in GeSn Layers with 6%−15% Sn Content. *Appl. Phys. Lett.* **2017**, *110*, 112101.
(41) Zheng, D. S.; Wang, J. L.; Hu, W. D.; Liao, L.; Fang, H. H.; Guo, N.; Wang, P.; Gong, F.; Wang, X. D.; Fan, Z. Y.; Wu, X.; Meng, X. J.; Chen, X. S.; Lu, W. When Nanowires Meet Ultrahigh Ferroelectric Field−High-Performance Full-Depleted Nanowire Photodetectors. *Nano Lett.* **2016**, *16*, 2548−2555.
(42) Zheng, D. S.; Fang, H. H.; Wang, P.; Luo, W. J.; Gong, F.; Ho, J. C.; Chen, X. S.; Lu, W.; Liao, L.; Wang, J. L.; Hu, W. D. High-Performance Ferroelectric Polymer Side-Gated CdS Nanowire Ultraviolet Photodetectors. *Adv. Funct. Mater.* **2016**, *26*, 7690−7696.
(43) Fang, C. Z.; Liu, Y.; Wang, Y. B.; Wu, J. B.; Han, G. Q.; Shao, Y.; Zhang, J. C.; Hao, Y. Buffer-Free GeSn with High Relaxation Degree Grown on Si(001) Substrate for Photodetection. *IEEE Photonics J.* **2018**, *10*, 1.
(44) Fang, H. H.; Hu, W. D.; Wang, P.; Guo, N.; Luo, W. J.; Zheng, D. S.; Gong, F.; Luo, M.; Tian, H. Z.; Zhang, X. T.; Luo, C.; Wu, X.; Chen, P. P.; Liao, L.; Pan, A. L.; Chen, X. S.; Lu, W. Visible Light-Assisted High-Performance Mid-Infrared Photodetectors Based on Single InAs Nanowire. *Nano Lett.* **2016**, *16*, 6416−6424.
(45) Su, M.; Yang, Z.; Liao, L.; Zou, X.; Ho, J. C.; Wang, J.; Wang, J.; Hu, W.; Xiao, X.; Jiang, C.; Liu, C.; Guo, T. Side-Gated In_2O_3 Nanowire Ferroelectric FETs for High-Performance Nonvolatile Memory Applications. *Adv. Sci.* **2016**, *3*, 1600078.

https://dx.doi.org/10.1021/acs.nanolett.0c01039
Nano Lett. 2020, 20, 3872−3879

Supporting Information for

Ferroelectric Enhanced Performance of GeSn/Ge Dual-nanowire Photodetector

Yuekun Yang[1,2], Xudong Wang[3], Chen Wang[1], Yuxin Song[1], Miao Zhang[1], Zhongying Xue[1], Shumin Wang[1], Zhongyunshen Zhu[1], Guanyu Liu[1], Panlin Li[1], Linxi Dong[4], Yongfeng Mei[5], Paul K. Chu[6], Weida Hu[3], Jianlu Wang[3*] & Zengfeng Di[1*]

[1]State Key Laboratory of Functional Materials for Informatics, Shanghai Institute of Microsystem and Information Technology, Chinese Academy of Sciences, Shanghai 200050, China

[2]Center of Materials Science and Optoelectronics Engineering, University of Chinese Academy of Sciences, Beijing 100049, China

[3]State Key Laboratory for Infrared Physics, Shanghai Institute of Technical Physics, Chinese Academy of Sciences, Shanghai 200083, China

[4]Key Laboratory of RF Circuits and System of Ministry of Education, College of

Electronic and Information, Hangzhou Dianzi University, Hangzhou 310018, China

[5]Department of Materials Science, State Key Laboratory of ASIC and Systems, Fudan University, Shanghai 200433, China

[6]Department of Physics, Department of Materials Science & Engineering, and Department of Biomedical Engineering, City University of Hong Kong, Tat Chee Avenue, Kowloon, Hong Kong, China

*Correspondence should be addressed to J.W. (email: jlwang@mail.sitp.ac.cn) or to Z.D. (email: zfdi@mail.sim.ac.cn)

This PDF file include:

Table S1. Brief review of photodetector devices built on different materials and structures

Year	Material	Structure	Cutoff (μm)	Dark Current	Reference
2012	GeSn/Ge	bulk	2.3	~0.5 mA	1
2013	InAs	NW	1.1	~2.5 nA	2
2014	InAs	NW	1.5	~0.5 nA	3
2014	GaAs/ AlGaAs	Core-shell NW	0.9	~10 pA	4
2016	GeSn	bulk	2.6	~0.6 mA	5
2016	InP	NW	1.0	~0.1 nA	6
2016	CdS	NW	0.7	~1 pA	6
2017	Ge	NW	1.6	~1 nA	7
2018	SnS	NW	1.1	~0.5 μA	8
2018	SnSe	NW	1.5	~0.25 μA	8
2018	GaAs	NW	0.9	~4 nA	9
2019	GaSb	NW	1.6	~0.4 μA	10
2020	GeSn/Ge	Dual-NW	2.2	~0.1 nA	this work

Supplementary Section I

Nanowire Synthesis

The GeSn/Ge dual-NWs were synthesized using DCA P450 MBE system via a two-step process. First, graphene was fully grown on Ge (110) via chemical vapor deposition (CVD) process, as reported previously[11]. Then, graphene-coated Ge substrate was smeared with several micrometer-thick In layer and put on a hot plate (200 ^{o}C). After heating for 2 minutes, In/graphene/Ge substrate was transferred into the MBE vacuum degassing chamber and baked at 500 ^{o}C for 60 minutes. Afterwards, the substrate was transferred into the MBE growth chamber and the first-step for Ge NW growth started with the Ge flow flux of 0.012 nm/s at 570 ^{o}C and continued for 150 minutes. It should be noted that the conjunction of graphene and several micrometer-thick In catalysis layer is essential for the successful growth of ultra-long Ge NW, as described in Figure S1. Compared to Au, In is able to provide the sufficient catalysis capability for Ge NW growth. In addition, due to the impermeability of graphene, the smeared In catalysis layer with sufficient thickness is unable to diffuse into the Ge substrate, thus avoiding the possible alloying process and sustaining the steady catalytic effect from In layer. After the growth of Ge NW, the second-step for GeSn overlayer growth subsequently started at 210 ^{o}C with Ge flux of 0.1 nm/s and Sn flux of 0.015 nm/s. The period for second-step growth was 850 s, which led to the formation of 100 nm-thick GeSn overlayer with Sn concentration of ~10% on the sidewall of Ge NW. Therefore, massive GeSn/Ge dual-NWs with the diameter ~150-200 nm and the length

8-10 μm can be obtained finally.

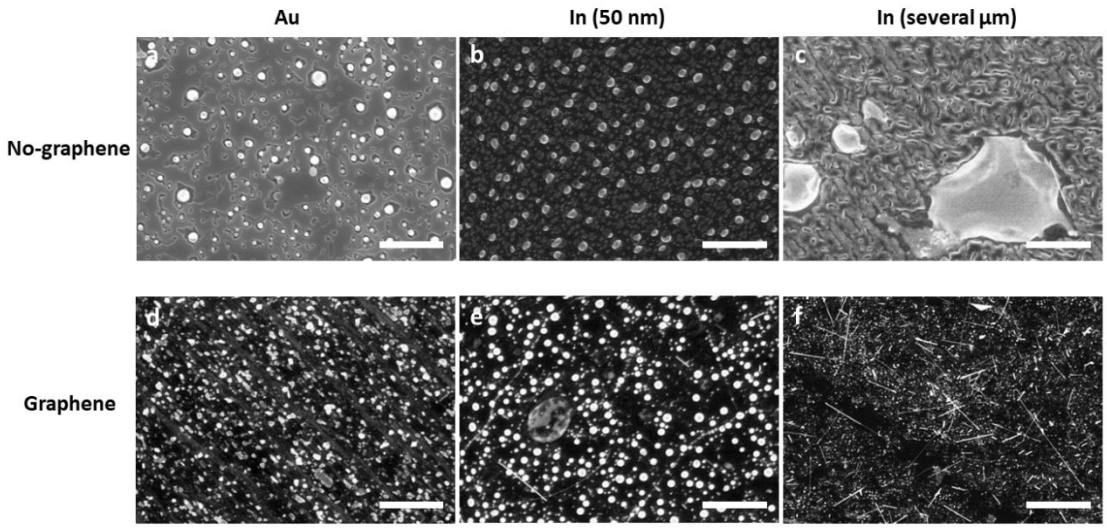

Supplementary Figure S1. SEM images of various substrates after Ge NW growth. (a) Au/Ge substrate without graphene. (b) 50 nm-thick MBE grown In/Ge substrate without graphene. (c) Several micrometer-thick smeared In/Ge substrate without graphene. (d) Au/graphene/Ge substrate. (e) 50 nm-thick MBE grown In/graphene/Ge substrate. (f) Several micrometer-thick smeared In/graphene/Ge substrate. It is observed that ultra-long Ge NW can only be obtained in (f), which is different from short and stumpy Ge NW grown via vapor-solid-solid (VSS) growth mode by MBE reported previously[12]. Scale bar, 5 μm in a-f.

Supplementary Section II

Characterization of Ge NW and GeSn/Ge Dual-NW

The cross-sectional TEM image of GeSn/Ge dual-NW on Cu grid is shown in Figure S2 (a). The yellow dashed rectangle denotes the contour of Ge NW core of GeSn/Ge dual-NW. The lateral size of GeSn/Ge dual-NW cross-section is ~150 nm. EDX spectrum collected from GeSn overlayer (red circle in Figure S2 (a)) depicts the presence of two dominant elements, i.e., Ge and Sn, as shown in Figure S2 (b). The inset table of Figure S2 (b) lists the measured atomic percentage of each element, which suggests that the Sn content in GeSn overlayer is ~10%. The signal of Cu is due to the Cu grid beneath the sample.

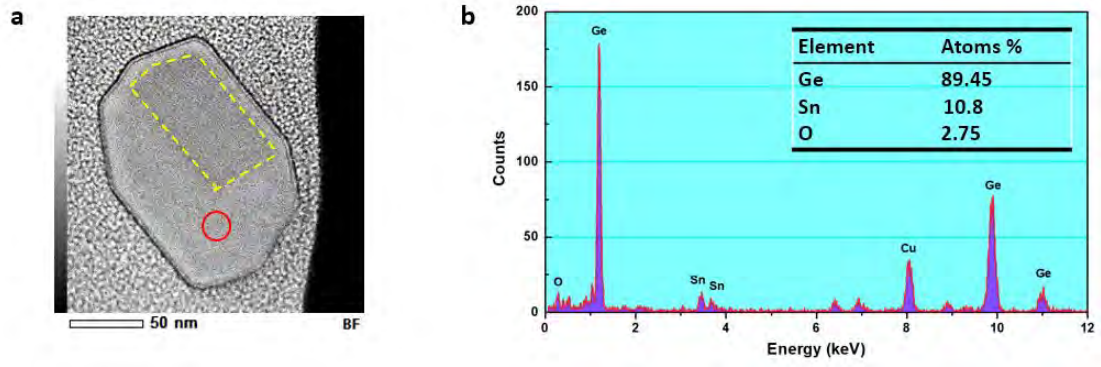

Supplementary Figure S2. Sn composition in GeSn/Ge dual-NW. (a) TEM image of the cross section of GeSn/Ge dual-NW. (b) The EDX spectrum collected from the GeSn overlayer, as denoted by red circle in (a). The inset table shows the measured atomic percentage of each element.

Figure S3 illustrates the SEM images and Raman spectroscopies of Ge NW and GeSn/Ge dual-NW. The surface morphologies of as-grown Ge NW and GeSn/Ge dual-NW are shown in Figure S3 (a) and S3 (d), respectively. The corresponding zoom-in

images of Ge NW and GeSn/Ge dual-NW are shown in S3 (b) and S3 (e), respectively. The diameter of Ge core NW is ~50-80 nm, and it increases to ~150-200 nm as GeSn/Ge dual-NW is formed. The lengths of Ge NW and GeSn/Ge dual-NW are about 8-10 μm. Ge NW is rather straight, suggesting no strain is residual. However, GeSn/Ge dual-NW is self-bended, indicating that the compressive strain in GeSn due to the lattice mismatch is relaxed during the formation of bended GeSn/Ge dual-NW. Raman spectra collected from Ge NW and GeSn/Ge dual-NW are shown in Figure S3 (c) and (f), respectively. It is found that the Ge-Ge LO-mode of Ge NW appears at ~301 cm^{-1}, whereas the Ge-Ge LO-mode of GeSn/Ge dual-NW emerges at ~295 cm^{-1}. A red shift of ~ 6 cm^{-1} is due to the incorporation of Sn into the GeSn overlayer of GeSn/Ge dual-NW, which corresponds to ~10% Sn content in GeSn[13,14].

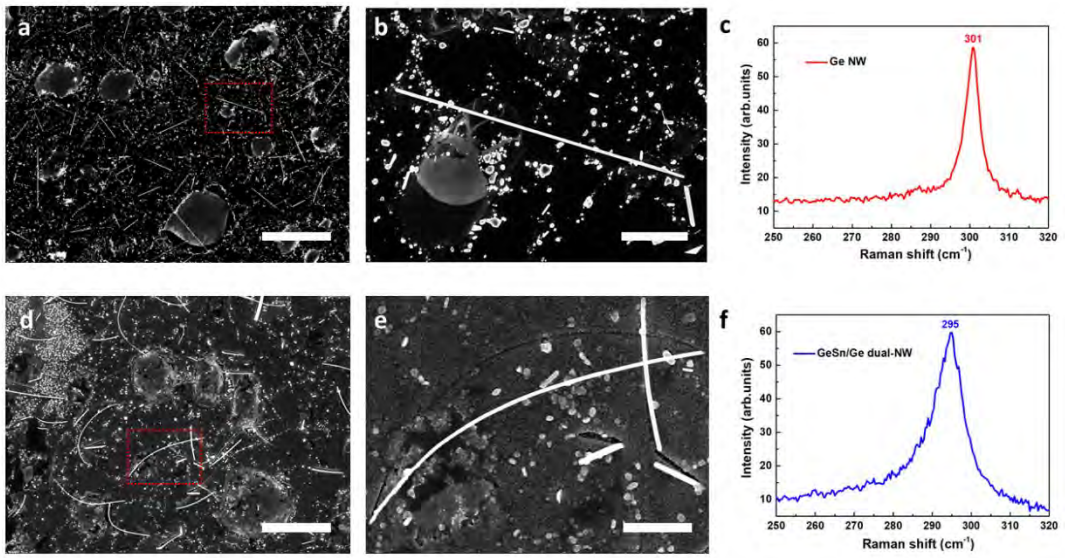

Supplementary Figure S3. Surface morphologies and Raman spectra of Ge NW and GeSn/Ge dual-NW. Top-view SEM image of as-grown Ge NW (a, b) and GeSn/Ge dual-NW (d, e). (b) A zoom-in image of red rectangle region in (a). (e) A zoom-in

image of red rectangle region in (d). Raman spectra of Ge NW (c) and GeSn/Ge dual-NW (f), respectively. Scale bar, 10 μm in a and d, 2 μm in b and e.

Supplementary References

(1) Gassenq, A.; Gencarelli, F.; Van Campenhout, J.; Shimura, Y.; Loo, R.; Narcy, G.; Vincent, B.; Roelkens, G. GeSn/Ge Heterostructure Short-wave Infrared Photodetectors on Silicon. *Opt. Express* **2012,** 20, 27297-27303.

(2) Liu, Z.; Luo, T.; Liang, B.; Chen, G.; Yu, G.; Xie, X.; Chen, D.; Shen, G. High-Detectivity InAs Nanowire Photodetectors with Spectral Response from Ultraviolet to Near-Infrared. *Nano Res.* **2013,** 6, 775-783.

(3) Miao, J.; Hu, W.; Guo, N.; Lu, Z.; Zou, X.; Liao, L.; Shi, S.; Chen, P.; Fan, Z.; Ho, J. C.; Li, T.-X.; Chen, X. S.; Lu, W. Single InAs Nanowire Room-Temperature Near-Infrared Photodetectors. *ACS Nano* **2014,** 8, 3628-3635.

(4) Dai, X.; Zhang, S.; Wang, Z.; Adamo, G.; Liu, H.; Huang, Y.; Couteau, C.; Soci, C. GaAs/AlGaAs Nanowire Photodetector. *Nano Lett.* **2014,** 14, 2688-2693.

(5) Pham, T.; Du, W.; Tran, H.; Margetis, J.; Tolle, J.; Sun, G.; Soref, R. A.; Naseem, H. A.; Li, B.; Yu, S.-Q. Systematic Study of Si-based GeSn Photodiodes with 2.6 μm Detector Cutoff for Short-wave Infrared Detection. *Opt. Express* **2016,** 24, 4519-4531.

(6) Zheng, D. S.; Wang, J. L.; Hu, W. D.; Liao, L.; Fang, H. H.; Guo, N.; Wang, P.; Gong, F.; Wang, X. D.; Fan, Z. Y.; Wu, X.; Meng, X. J.; Chen, X. S.; Lu, W. When Nanowires Meet Ultrahigh Ferroelectric Field–High-Performance Full-Depleted Nanowire Photodetectors. *Nano Lett.* **2016,** 16, 2548-2555.

(7) Otuonye, U.; Kim, H. W.; Lu, W. D. Ge Nanowire Photodetector with High

Photoconductive Gain Epitaxially Integrated on Si Substrate. *Appl. Phys. Lett.* **2017,** 110, 173104.

(8) Zheng, D. S.; Fang, H. H.; Long, M. S.; Wu, F.; Wang, P.; Gong, F.; Wu, X.; Ho, J. C.; Liao, L.; Hu, W. D. High-Performance Near-Infrared Photodetectors Based on P-Type SnX (X = S, Se) Nanowires Grown via Chemical Vapor Deposition. *ACS Nano* **2018,** 12, 7239-7245.

(9) Ali, H.; Zhang, Y. Y.; Tang, J.; Peng, K.; Sun, S. B.; Sun, Y.; Song, F. L.; Falak, A.; Wu, S. Y.; Qian, C. J.; Wang, M.; Zuo, Z. C.; Jin, K. J.; Sanchez, A. M.; Liu, H. Y.; Xu, X. L. High-Responsivity Photodetection by a Self-Catalyzed Phase-Pure P-GaAs Nanowire. *Small* **2018,** 14, 1704429.

(10) Sun, J.; Peng, M.; Zhang, Y.; Zhang, L.; Peng, R.; Miao, C.; Liu, D.; Han, M.; Feng, R.; Ma, Y.; Dai, Y.; He, L.; Shan, C.; Pan, A.; Hu, W.; Yang, Z.-x. Ultrahigh Hole Mobility of Sn-Catalyzed GaSb Nanowires for High Speed Infrared Photodetectors. *Nano Lett.* **2019,** 19, 5920-5929.

(11) Wang, G.; Zhang, M.; Zhu, Y.; Ding, G. Q.; Jiang, D.; Guo, Q. L.; Liu, S.; Xie, X. M.; Chu, P. K.; Di, Z. F.; Wang, X. Direct Growth of Graphene Film on Germanium Substrate. *Sci. Rep.* **2013,** 3, 2465.

(12) Zhu, Z.; Song, Y.; Zhang, Z.; Sun, H.; Han, Y.; Li, Y.; Zhang, L.; Xue, Z.; Di, Z.; Wang, S. Vapor-Solid-Solid Grown Ge Nanowires at Integrated Circuit Compatible Temperature by Molecular Beam Epitaxy. *J. Appl. Phys.* **2017,** 122, 094304.

(13) Han, D.; Ye, H.; Song, Y.; Zhu, Z.; Yang, Y.; Yu, Z.; Liu, Y.; Wang, S.; Di, Z.

Analysis of Raman Scattering from Inclined GeSn/Ge Dual-Nanowire Heterostructure on Ge(111) Substrate. *Appl. Surf. Sci.* **2019,** 463, 581-586.

(14) Gassenq, A.; Milord, L.; Aubin, J.; Pauc, N.; Guilloy, K.; Rothman, J.; Rouchon, D.; Chelnokov, A.; Hartmann, J.; Reboud, V. Raman Spectral Shift versus Strain and Composition in GeSn Layers with 6%–15% Sn Content. *Appl. Phys. Lett.* **2017,** 110, 112101.